

## Supporting Information

# Interaction-Dependent Interfacial Charge Transfer Behavior in Solar Water Splitting Systems

Guancai Xie,<sup>†,‡,§</sup> Liming Guan,<sup>†,§</sup> Linjuan Zhang,<sup>||,§</sup> Beidou Guo,<sup>†,‡</sup> Aisha Batool,<sup>†,‡</sup> Qi Xin,<sup>†</sup>  
Rajender Boddula,<sup>†,‡</sup> Saad Ullah Jan,<sup>†,‡</sup> and Jian Ru Gong<sup>\*,†</sup>

<sup>†</sup>Chinese Academy of Sciences (CAS) Key Laboratory for Nanosystem and Hierarchical  
Fabrication, CAS Center for Excellence in Nanoscience, National Center for Nanoscience and  
Technology, Beijing 100190, P. R. China

<sup>‡</sup>University of Chinese Academy of Sciences, Beijing 100049, P. R. China

<sup>||</sup> Shanghai Institute of Applied Physics, CAS, Shanghai 201800, P. R. China

\* gongjr@nanoctr.cn

## Experimental Section

### Sample preparation

All reagents were of analytical grade and used without further purification. Graphene oxide (GO) was prepared from graphite flakes (> 99.8%, Alfa Aesar) by a modified Hummers' method.<sup>1</sup> An aqueous GO dispersion (0.125 mg mL<sup>-1</sup>) was prepared by ultrasonication and stored for further use. To synthesize CdS/GO nanocomposites, 2.5 mmol of Cd(Ac)<sub>2</sub>•2H<sub>2</sub>O (~98.5%, Aladdin) was dispersed in 40 mL of aqueous GO solution. After vigorous stirring for 6 h, 20 mL of Na<sub>2</sub>S solution (0.125 M) was added dropwise into the suspension and stirred for another 24 h. The precipitate obtained was washed three times successively with ethanol and deionized water, followed by drying in an oven at 60 °C for 12 h.

RGO was prepared by reduction under hydrothermal conditions. The degree of reduction of GO in the as-prepared CdS/GO composites was tuned by varying the volume of hydrazine hydrate (N<sub>2</sub>H<sub>4</sub>•H<sub>2</sub>O), used as the reducing agent in the hydrothermal treatment. Typically, CdS/GO composites were re-dispersed in 40 mL of deionized water containing various volumes of N<sub>2</sub>H<sub>4</sub>•H<sub>2</sub>O. The suspension was then transferred into a 50 mL Teflon-lined autoclave and subjected to hydrothermal treatment at 80 °C for 1 h. The final product was collected by centrifugation, washed repeatedly with deionized water, and dried at 60 °C. Depending on the volume of N<sub>2</sub>H<sub>4</sub>•H<sub>2</sub>O used, the obtained samples were labeled as Cg<sub>0</sub>, Cg<sub>1</sub>, Cg<sub>2</sub>, Cg<sub>3</sub>, and Cg<sub>4</sub>, corresponding, respectively, to N<sub>2</sub>H<sub>4</sub>•H<sub>2</sub>O volumes of 0, 10, 50, 500, and 2000 μL. For comparison, hydrothermally-treated pure CdS was also synthesized using the same procedure described above, but without the addition of GO or hydrazine hydrate.

### Sample characterization

The crystal structures of the samples were identified by X-ray diffraction (XRD) using D/MAX-2500 diffractometer (Rigaku, Japan) with Cu Kα radiation source ( $\lambda = 1.54056 \text{ \AA}$ ). Field emission scanning electron microscopy (FESEM, Hitachi S4800) and transmission electron microscopy (TEM, G2 F20, FEI co.) were employed to characterize the morphology of the samples. Raman spectra were recorded on a Renishaw InVia Plus laser Raman spectrometer at room temperature using the 514 nm line of an Ar<sup>+</sup>-ion laser as the excitation source. The Brunauer-Emmett-Teller (BET) specific surface area of the powders was analyzed by nitrogen

adsorption in a NOVA3200e nitrogen adsorption apparatus. All of the prepared samples were degassed at 200 °C prior to nitrogen adsorption measurements. The BET surface area was determined by a multi-point BET method using the adsorption data in the relative pressure ( $P/P_0$ ) range of 0.04–0.3. UV-visible diffuse reflectance spectra (DRS) were taken on a Cary 5000 spectrophotometer in the range of 300–800 nm using an integrating sphere accessory normalized against MgO standard. Photoluminescence (PL) spectra were taken on an FLS920 fluorescence spectrometer (Edinburgh Instruments) in air at room temperature under 217 nm excitation. X-ray photoelectron spectroscopy (XPS) was conducted with an ESCALAB250Xi using 300 W Al K $\alpha$  radiation; the base pressure was  $\sim 3 \times 10^{-9}$  mbar. Binding energies were referenced to the C 1s line at 284.8 eV from adventitious carbon. To calculate the C/O ratio in RGO for the different composites, XPS spectra were recorded on bare RGO samples obtained after dissolving the CdS nanoparticles in the composites with dilute HCl. Surface photovoltage (SPV) measurements were carried out using a home-built instrument similar to that described elsewhere.<sup>2</sup> During the experiment, the sample was inserted between indium tin oxide and stainless-steel electrodes to form a sandwich-like photovoltage cell; the thickness of the samples was maintained constant for all the measurements.

### **X-ray absorption spectroscopic measurements**

X-ray absorption fine structure (XAFS) data were collected at the HXMA beamline (06-ID1) of the Canadian Light Source with a Si (111) double crystal monochromator in transmission mode for the Cd K-edge. The electron beam energy of the storage ring was 2.9 GeV and the maximum stored current was  $\sim 250$  mA. Cd K-edge XAFS data were analyzed using standard procedures in Demeter, which is a comprehensive system for processing and analyzing X-ray Absorption Spectroscopy data.<sup>3</sup> Theoretical phase and amplitude functions were calculated from the program FEFF 9.0.<sup>4</sup> Fitting procedures were performed on  $k^2$ -weighted FT-EXAFS from 3 to 12 Å<sup>-1</sup> using R window of 1–3 Å for fitting. The amplitude reduction factor  $S_0^2$  was fixed at 1 in EXAFS fits, and the shifts in the threshold energy  $\Delta E_0$  were constrained to be the same value for all fitted shells. The coordination numbers ( $N$ ), interatomic distances ( $R$ ), and the Debye-Waller factors ( $\Delta\sigma^2$ ) were left as free parameters.

### Photocatalytic hydrogen generation

Photocatalytic hydrogen generation reactions were conducted in a top-irradiation type Pyrex vessel connected to a glass closed circulation system. A 350 W xenon arc lamp with a UV cut-off filter ( $\lambda > 420$  nm) was used to ensure that only visible light passed through. In a typical photocatalytic experiment, 20 mg of the photocatalyst was dispersed under constant stirring in 80 mL of 0.1M Na<sub>2</sub>S/0.1M Na<sub>2</sub>SO<sub>3</sub> aqueous solution contained in the reactor, which was placed in a thermostat with water circulation so as to maintain the temperature at  $25 \pm 2$  °C in a thermostat. Before irradiation, the system was evacuated several times by a mechanical pump to completely remove air in the reactor as well as in the solution. The generated hydrogen was analyzed by online gas chromatography (GC7890II, Shanghai Techcomp Limited, China, TCD, using argon as the carrier gas and a 5 Å molecular sieve column).

### Model and computational details

Five models of CdS/RGO systems with different reduction levels of graphene oxide were introduced to reveal how reduction level affects the interfacial charge transfer between CdS and RGO. A CdS cluster with four Cd and four S was used;<sup>5</sup> after structural relaxation, the cluster was deposited above a 5×5 graphene supercell. Next, 0, 1, 3, 6, and 10 hydroxyl groups were added onto the graphene to model RGO with different reduction degrees; these were labeled CG<sub>0</sub>, CG<sub>1</sub>, CG<sub>2</sub>, CG<sub>3</sub>, and CG<sub>4</sub>, respectively. We also added a vacuum layer to each model so that all the model supercells had a height of 20 Å. All the calculations were performed using Vienna *ab initio* simulation package (VASP) with the exchange and interaction potentials described by the Perdew-Burke-Ernzerhof (PBE) of the generalized gradient approximation and Hubbard on-site potential (GGA+U).<sup>6, 7</sup> Van der Waals (vdW) correction was adopted to describe long-range vdW interactions and dipole-dipole interaction was employed due to the asymmetric layer-cluster arrangement. The cutoff energy of the electronic wave-function was 600 eV, and the *k*-space integration was done with a 5×5×1 *k*-mesh in the Monkhorst-Park scheme. Geometry optimization of the above five models was terminated when the force on each ion was no stronger than 0.05 eV Å<sup>-1</sup>. The interacting strength between RGO sheets and CdS cluster can be read from the binding energy  $E_b = E_{\text{CdS/RGO}} - E_{\text{CdS}} - E_{\text{RGO}}$ , where  $E_{\text{CdS/RGO}}$ ,  $E_{\text{CdS}}$ , and  $E_{\text{RGO}}$  denote the total energies of the CdS/RGO system, CdS cluster and an isolated RGO sheet, respectively. The charge density difference between the models was calculated according to the equation:  $\Delta\rho$

$= \rho_{\text{CdS/RGO}} - \rho_{\text{CdS}} - \rho_{\text{RGO}}$ , where  $\rho_{\text{CdS/RGO}}$ ,  $\rho_{\text{CdS}}$ , and  $\rho_{\text{RGO}}$  are, respectively, the charge densities of the CdS/RGO system, CdS cluster and an isolated RGO sheet of the same configuration.

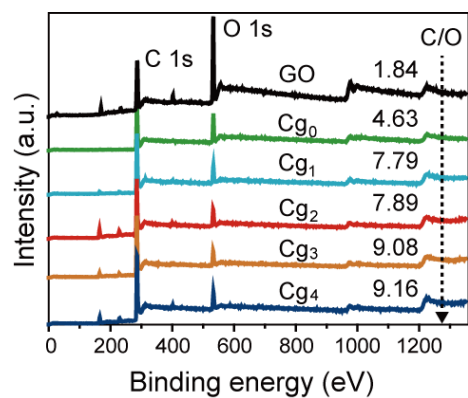


**Figure S1.** XPS survey spectra of GO and RGO in CdS/RGO composites, showing a gradual increase in RGO reduction from Cg<sub>0</sub> to Cg<sub>4</sub>, as the C/O ratio increases from 4.63 for Cg<sub>0</sub> to 9.16 for Cg<sub>4</sub>, owing to the gradual removal of oxygen-containing groups.

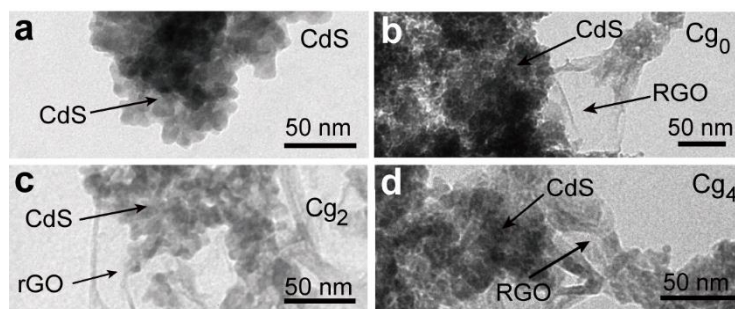


**Figure S2.** TEM images of (a) bare CdS, (b) Cg<sub>0</sub>, (c) Cg<sub>2</sub>, and (d) Cg<sub>4</sub> samples.

TEM images show that aggregated CdS particles are deposited onto RGO sheets. The aggregation of CdS nanocrystals might be due to their high surface free energy, leading to inter particle collision through Brownian motion, finally forming large particles via van der Waals attraction.<sup>8-10</sup> No obvious change in the morphology of the CdS/RGO nanocomposites with different degree of RGO reduction is observed. Thus, the reduction process has little effect on the morphology of CdS/RGO composites.

Although the average grain size derived from XRD patterns is as small as  $\sim 2.2 \pm 0.2$  nm, the size of most aggregated CdS particle is  $>50$  nm. It should be noted that the grain size is different from the particle size because the particles of polycrystalline materials (such as CdS in our case) always consists of many grains.

## Band Bending in the Photocatalysts

The total potential drop  $\Delta\phi$  within a CdS particle can be calculated according to the following equation:<sup>11</sup>

$$\Delta\phi = \frac{k_B T}{6e} \left( \frac{r}{L_D} \right)^2 \quad (\text{S1})$$

where  $k_B$  is the Boltzmann constant,  $T$  is the absolute temperature in Kelvin,  $r$  is the radius of the particle, and  $L_D = (\epsilon_0 \epsilon k_B T / 2e^2 N_D)^{0.5}$  is the Debye length. With the dielectric constant ( $\epsilon$ ) and ionized donor concentration ( $N_D$ ) values of 8.9 and  $10^{17} \text{ cm}^{-3}$ ,<sup>12, 13</sup> respectively, and the Debye length is 8 nm, the potential drop between the surface and the center of the particle is as high as 42 mV for a 50-nm size CdS particle. This high value for the potential drop suggests that band bending within the CdS particles has a non-negligible effect on the interfacial charge transfer process.



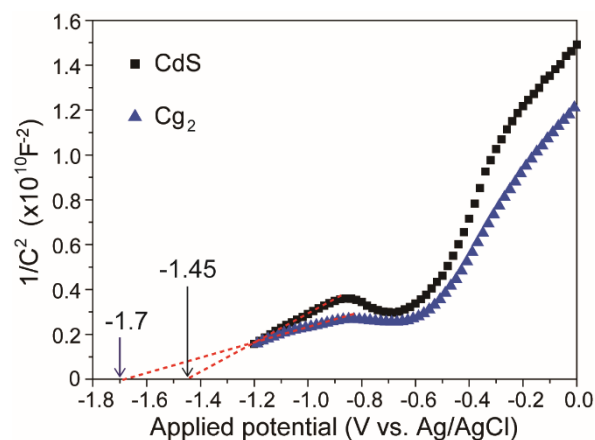


**Figure S3.** Mott-Schottky plots for CdS and Cg<sub>2</sub> samples loaded on ITO in 0.1 M Na<sub>2</sub>S/0.1M Na<sub>2</sub>SO<sub>3</sub> aqueous electrolyte. In a previous report on CdSe nanoribbon photocatalysts,<sup>14</sup> the flat-band potential of CdSe was found to be fixed at a potential slightly below the sulfide redox potential in the presence of a sulfide ion; this was attributed to the adsorption of the hydrosulfide on the surface of the semiconductor. The Mott-Schottky plots given above show that the flat-band potential of Cg<sub>2</sub> is about 0.25 V more negative than that of the bare CdS, thus ruling out a fixed flat-band potential for the CdS/RGO nanocomposites.

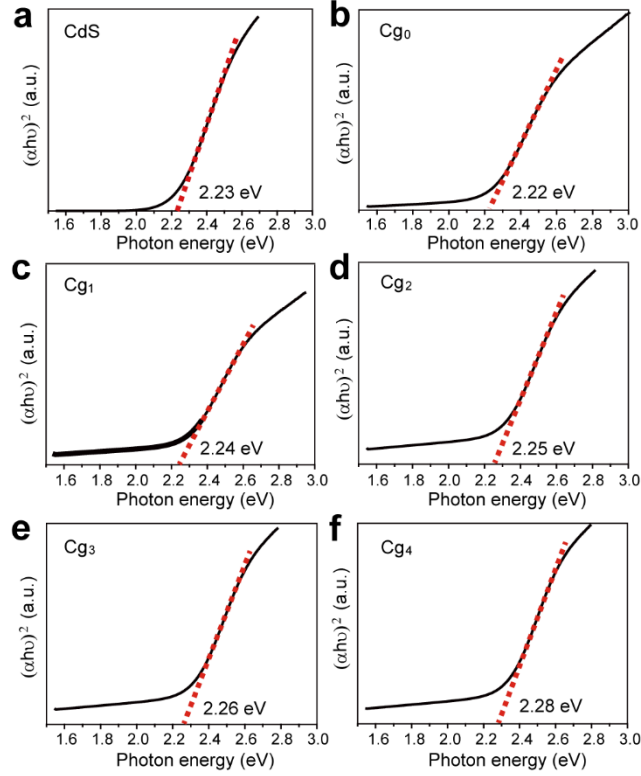


**Figure S4.** Determination of bandgap using the Tauc plot for (a) CdS, (b) Cg<sub>0</sub>, (c) Cg<sub>1</sub>, (d) Cg<sub>2</sub>, (e) Cg<sub>3</sub>, and (f) Cg<sub>4</sub>

The optical bandgap ( $E_g^{opt}$ ) of a direct bandgap semiconductor like CdS can be obtained by using the Tauc relation:<sup>15</sup>

$$\alpha h\nu \propto B(h\nu - E_g^{opt})^{1/2} \quad (S2)$$

where  $\alpha$  is the absorption coefficient,  $B$  is a constant, and  $h\nu$  is the photon energy. The bandgap of the sample is estimated by extrapolating the linear region of the plot of the square of the absorbance against the photon energy, i.e., the intercept of the red dotted-line on the  $x$ -axis (Figure S4).

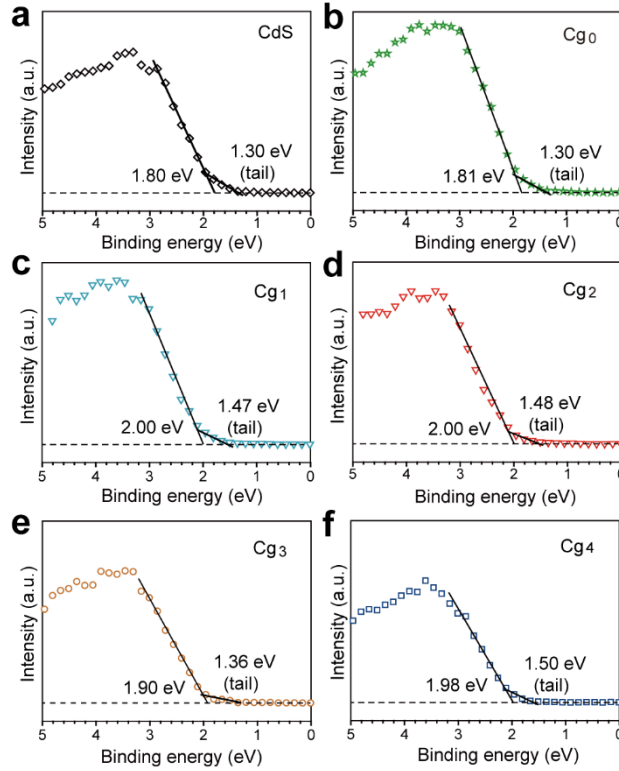


**Figure S5.** Valence band XPS spectra of (a) CdS, (b) Cg<sub>0</sub>, (c) Cg<sub>1</sub>, (d) Cg<sub>2</sub>, (e) Cg<sub>3</sub>, and (f) Cg<sub>4</sub>. The VB maximum energy and the band tail of the sample are marked in each plot.

Considering the exponential absorption tails observed below the absorption edge in Figure S4, we infer that the shrinking of the bandgap in our samples is presumably due to the presence of band tails in the bandgap of CdS, which is confirmed by the valence band XPS of the samples given in Figure S5.<sup>16-18</sup>

It is clearly seen in Figure S5 that the VB maximum energies of all the samples are followed by a band tail known as the Urbach tail. The presence of the Urbach tail allows the material to absorb photons with energies below its bandgap. Two reasons have been proposed to explain the origin of the Urbach tail, namely, electron-phonon coupling and the presence of structural disorders (impurities, defects, grain boundaries, *etc.*).<sup>19, 20</sup> Electron-phonon coupling can extend the density of states from the band edges into the bandgap, while structural disorders can form groups of localized states near the band edges; both effects can lead to bandgap shrinking.

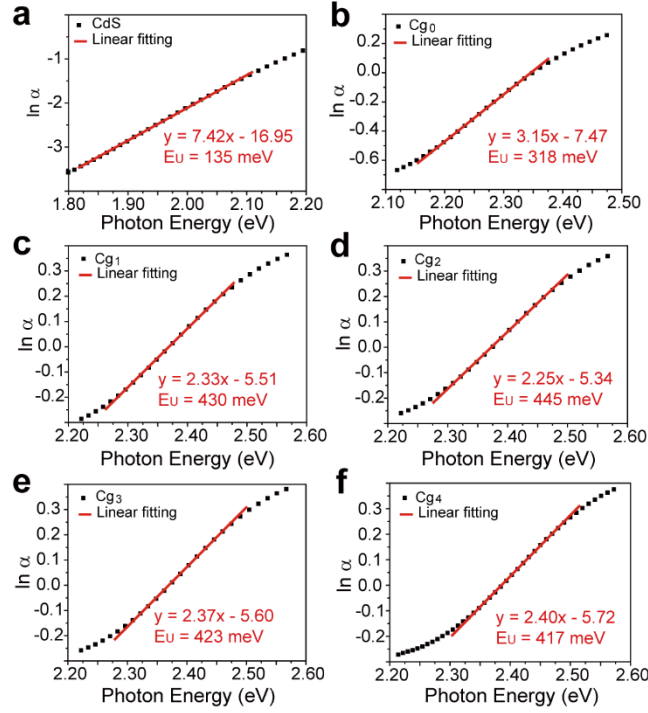


**Figure S6.** Variation of absorption coefficient with photon energy for: (a) CdS, (b) Cg<sub>0</sub>, (c) Cg<sub>1</sub>, (d) Cg<sub>2</sub>, (e) Cg<sub>3</sub>, and (f) Cg<sub>4</sub>. The Urbach energy is obtained from the slope of the linear fit of the experimental data.

Band tailing in semiconductors is characterized by Urbach energy. In the presence of band tailing, at the absorption edge, the absorption coefficient shows an exponential increase with photon energy instead of a steep rise, and obeys the Urbach rule expressed by the following equation:<sup>20</sup>

$$\alpha = \alpha_0 e^{(E-E_0/E_U)} \quad (S3)$$

where  $\alpha_0$  and  $E_0$  are characteristic parameters of the material,  $\alpha$  is the absorption coefficient, and  $E$  and  $E_U$  are the photon energy and Urbach energy, respectively. Thus, the value of  $E_U$  can be estimated by taking the reciprocal of the slope of the linear portion of the plot of  $\ln(\alpha)$  against photon energy in the lower photo energy region (with photon energies smaller than the theoretical bandgap).

Figure S6 shows that the values of  $E_U$  for both bare CdS and CdS/RGO nanocomposites are much bigger than the previously reported value for bulk CdS (16 meV).<sup>21</sup> Considering that the

optical bandgaps of all CdS/RGO samples are smaller than that of bulk CdS (2.42 eV) and that Urbach tails are present in the samples, we can infer that the measured optical bandgaps are actually due to charge transitions involving band tails instead of transitions from the VB to the CB.<sup>22</sup>

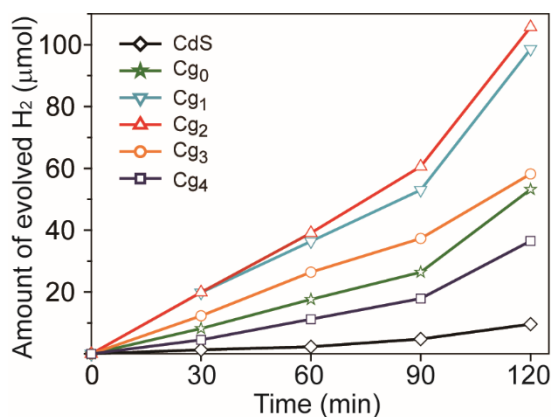


**Figure S7.** The time courses of H<sub>2</sub> production of the samples. 0.1 M Na<sub>2</sub>S/0.1M Na<sub>2</sub>SO<sub>3</sub> solution was used as the sacrificial reagent; a 350 W xenon arc lamp with a 420 nm cutoff filter was used as the light source. The data show that the amount of H<sub>2</sub> evolved over each catalyst increases proportionally with the reaction time, indicating that H<sub>2</sub> was produced by photocatalytic reactions on the photocatalysts.<sup>23</sup>

## Other factors that possibly influence photocatalytic activity

### 1. Residual hydrazine

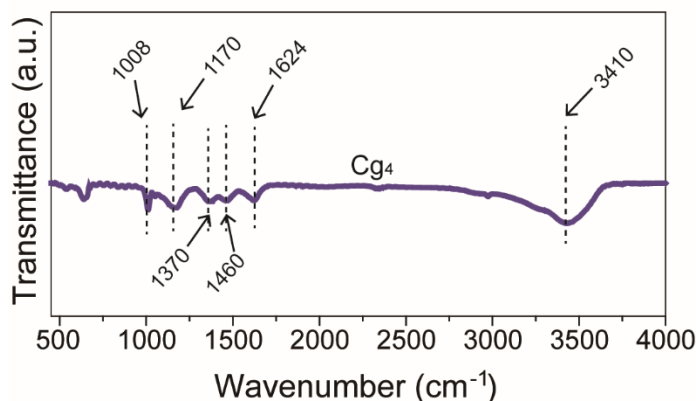


**Figure S8.** FTIR spectrum of Cg<sub>4</sub>

FTIR spectroscopy was used to confirm the absence of residual hydrazine in our samples. Cg<sub>4</sub> sample was measured because the largest amount of hydrazine was used in its synthesis. As shown in Figure S8, there are peaks centered at 1008, 1170, 1624, and 3410 cm<sup>-1</sup>, corresponding to epoxy C-O stretching, alkoxy C-O stretching, aromatic C=C stretching and O-H bending, and C-OH stretching, respectively.<sup>24, 25</sup> The peaks centered at 1370 and 1460 cm<sup>-1</sup> are assigned to vibration modes due to C-O, which might be produced during the decomposition of C=O and epoxy groups in GO by hydrazine reduction.<sup>24</sup> No peaks corresponding to NH<sub>2</sub> group are observed in the FTIR spectrum of Cg<sub>4</sub>, indicating that there is little residual hydrazine in the photocatalysts. In addition, hydrazine is a commonly used reducing agent for GO, and has also been widely used for the synthesis of graphene-based photocatalysts.<sup>26-28</sup> To the best of our knowledge, the effects of residual hydrazine on the photocatalytic activity of graphene-based photocatalysts have not been reported. Based on the above results, we can rule out the possible influence of residual hydrazine on the activity of the composites.

### 2. Solubility of RGO

One may also suspect that the variation in H<sub>2</sub> evolution rates is due to changes in aggregation of the CdS/GO composites, caused by the change in solubility of RGO with degree of reduction. Although the solubility of GO is lowered after reduction, we did not observe any significant difference in the morphology of the different CdS/RGO samples from TEM images (Figure S2).

Besides, if aggregation affects the photocatalytic activity of CdS/RGO composites, a continuous decline in photocatalytic activity can be expected from Cg<sub>0</sub> to Cg<sub>4</sub> due to the increasing aggregation of the composites, but this is not the case, with Cg<sub>2</sub> having the highest photocatalytic activity. Furthermore, the weight ratio of GO to the composite is only 1%, so its aggregation is not expected to significantly affect photocatalytic performance. In short, the solubility of RGO is not a major factor that affects the activity of CdS/GO composites.

### 3. Specific surface area

**Table S1** Specific surface area ( $S_{\text{BET}}$ ) of the CdS/RGO photocatalysts

Sample	$S_{\text{BET}}$ (m <sup>2</sup> g <sup>-1</sup> )
CdS	126.6
Cg <sub>0</sub>	109.2
Cg <sub>1</sub>	125.2
Cg <sub>2</sub>	87.5
Cg <sub>3</sub>	91.3
Cg <sub>4</sub>	143.3

Usually, the photocatalyst with a larger specific surface area provides more surface-active sites, leading to an enhancement of the photocatalytic performance.<sup>29</sup> In our case, there is no direct correlation between the specific surface area ( $S_{\text{BET}}$ ) and the photocatalytic activity. For example, the Cg<sub>2</sub> sample, which shows the best photocatalytic activity, has the lowest  $S_{\text{BET}}$ , suggesting that the specific surface area does not play a dominant role in increasing or decreasing the photocatalytic activity of our samples.

#### 4. Heating effect of RGO

The absorption in the visible and infrared region of RGO has been previously attributed to the electronic  $\pi$ -conjugation within the graphene sheets, and the absorption intensity was found to be directly related to the degree of  $\pi$ -conjugation in RGO.<sup>30-32</sup> For RGO with a low reduction degree, the  $\pi$ -conjugation is severely disrupted, which results in low optical absorption in the red region (600–800 nm). Chemical reduction by hydrazine restores part of the  $\pi$ -conjugation and results in increased absorption and therefore, a strong offset in the red part of the absorption spectrum was observed between Cg<sub>0</sub> and Cg<sub>1</sub>. With further reduction, the degree of  $\pi$ -conjugation in RGO did not change significantly and as a result, the absorption enhancement from Cg<sub>1</sub> to Cg<sub>4</sub> was very small. Previous reports also suggest that Joule heating due to the visible light absorption of RGO might promote hydrogen evolution reaction to some extent.<sup>33</sup> In our case, Cg<sub>1</sub>, Cg<sub>2</sub>, Cg<sub>3</sub>, and Cg<sub>4</sub> show similar broad absorption in the range of 600–800 nm, which excludes the role of “heating effect” on the photocatalytic activity, since heating effect cannot explain the decreased activity of Cg<sub>3</sub> and Cg<sub>4</sub>.



**Table S2** A summary of the elemental composition determined from XPS of the various samples

Sample	Content (At. %)		Cd/S
	Cd	S	
CdS	27.27	24.59	1.1
Cg <sub>0</sub>	28.06	23.32	1.2
Cg <sub>1</sub>	23.80	19.96	1.2
Cg <sub>2</sub>	24.08	19.93	1.2
Cg <sub>3</sub>	32.83	26.81	1.2
Cg <sub>4</sub>	31.57	26.76	1.2

Table S2 shows that the Cd<sup>2+</sup> content is higher than that of S<sup>2-</sup> in all our samples, which indicates that both bare CdS and CdS/RGO composites are sulfur-deficient.<sup>34, 35</sup>

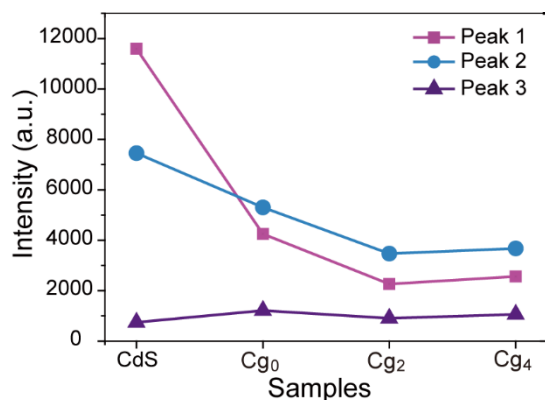


**Figure S9.** PL intensities of Peak1, Peak2, and Peak3 for CdS, Cg<sub>0</sub>, Cg<sub>2</sub>, and Cg<sub>4</sub>.

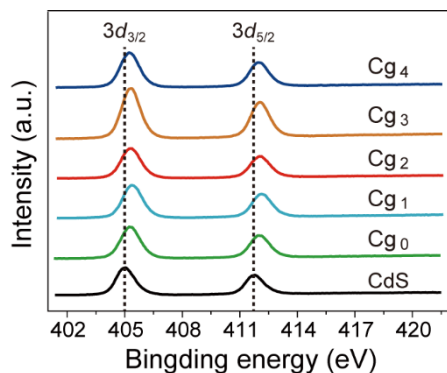


**Figure S10.** High-resolution Cd 3d XPS spectra of the samples. The Cd 3d spectra show a doublet due to spin-orbit coupling, corresponding to 3d<sub>3/2</sub> and 3d<sub>5/2</sub> peaks with a spin-orbit splitting energy of 6.7 eV. For bare CdS, signals at 405 and 411.7 eV are attributed to Cd 3d<sub>3/2</sub> and Cd 3d<sub>5/2</sub> binding energies, respectively. The two spin-orbit components of Cd 3d in all CdS/RGO nanocomposites shift towards higher binding energies compared to those of bare CdS. RGO with a higher density of oxygen-containing groups can form stronger interactions with semiconductors when coated on the surface, since oxygen-containing groups are generally considered to be anchoring sites for semiconductors.<sup>36, 37</sup> It has been reported<sup>38</sup> that the shift in binding energy observed for the CdS/RGO composites is due to electrostatic interaction between CdS and RGO.

**Table S3** Parameters of local structure around Cd atoms obtained from a curve fit of the Cd K-edge EXAFS spectra

Sample	Bond type	$N^a$	$R$ (Å) <sup>b</sup>	$\sigma^2 \times 10^{-3}$ (Å <sup>2</sup> ) <sup>c</sup>
CdS	Cd-S	4.0	2.53±0.01	6.7±0.4
Cg <sub>0</sub>	Cd-S	3.7±0.4	2.51±0.01	6.6±0.8
Cg <sub>1</sub>	Cd-S	3.9±0.4	2.52±0.01	7.2±0.9
Cg <sub>2</sub>	Cd-S	4.0±0.4	2.52±0.01	7.4±0.8
Cg <sub>3</sub>	Cd-S	4.0±0.2	2.53±0.01	7.4±0.7
Cg <sub>4</sub>	Cd-S	4.1±0.3	2.53±0.01	7.8±0.8

<sup>a</sup> $N$  is the coordination number, <sup>b</sup> $R$  is the distance between Cd atoms and the surrounding S atoms, <sup>c</sup> $\sigma^2$  is the Debye-Waller factor serving as a measure of local disorder.

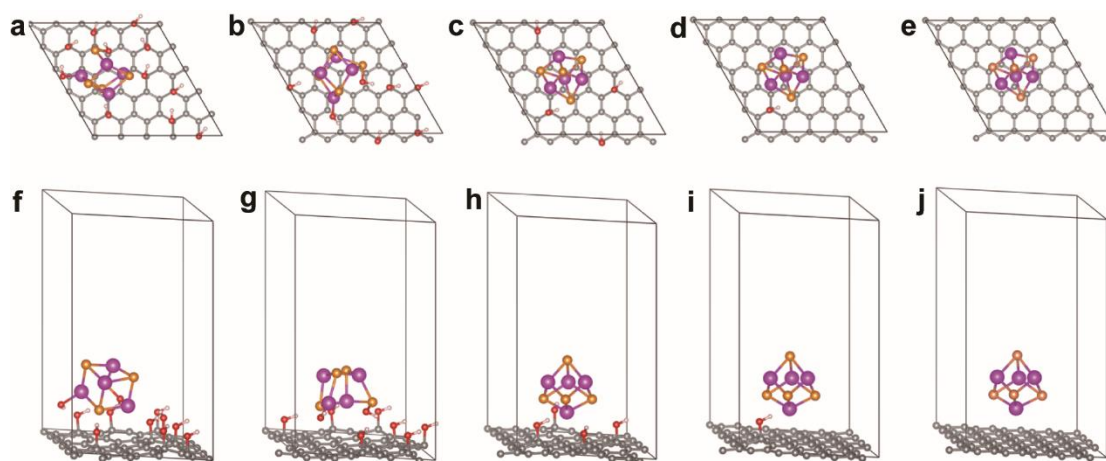


**Figure S11.** Top-view and side-view of the optimized geometries of the composites (a,f) CG<sub>0</sub>, (b,g) CG<sub>1</sub>, (c,h) CG<sub>2</sub>, (d,i) CG<sub>3</sub>, and (e,j) CG<sub>4</sub>. Gray, red, pink, purple, and orange spheres denote carbon, oxygen, hydrogen, cadmium, and sulfur atoms, respectively.

## Interfacial Charge Transfer

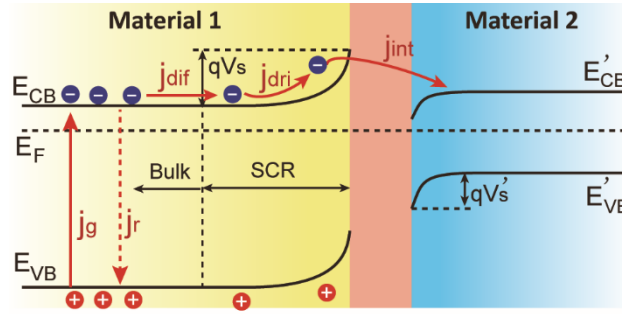


**Figure S12.** Schematic showing electron transfer processes taking place in a dual-band-gap system. SCR represents space charge region,  $j_g$ ,  $j_r$ ,  $j_{dif}$ ,  $j_{dri}$ , and  $j_{int}$  are, respectively, the photon-generated current, recombination current, drift current, diffusion current, and interfacial transfer current,.

For convenience, the material at the left of the interface in the dual-band-gap system is labeled as Material 1 and that at the right is labeled as Material 2, as depicted in Figure S12. The electron flux flowing from Material 1 to Material 2 is proportional to the product of the number of electron donors in Material 1 and the number of electron acceptors in Material 2. Similarly, the flux flowing from Material 2 to Material 1 is proportional to the product of the number of donors in Material 2 and acceptors in Material 1. As the charge transfer behaviors in Material 1 and Material 2 are similar and the electron and hole have similar transfer behavior, we first consider electron transfer (ET) in the following discussion.

For equilibrium and quasi-equilibrium cases, the steady-state charge transport equation for electrons in Material 1 is:

$$D_n \frac{\partial^2 n}{\partial x^2} + \mu_n \frac{\partial}{\partial x} \left( n \frac{\partial \Phi}{\partial x} \right) + g(x) - r(x) - a \delta_{x,0} = 0 \quad (\text{S4})$$

where  $D_n$  is the diffusion coefficient of electrons,  $\mu_n$  is the mobility of electrons,  $\Phi$  is the electronic potential,  $x$  is the position (set to be 0 at the interface),  $n$  is the bulk electron concentration,  $g$  is the photon-induced electron-hole pair generation rate,  $r$  is the recombination rate,  $a$  is the interfacial electron transfer rate,  $\delta_{x,0}$  is a Dirac function, which is 1 for  $x = 0$  and 0 for others. Each of the terms in Equation S4 represents the diffusion current, the drift current, the

photon-generated current, the recombination current, and the interfacial transfer current, as illustrated in Figure S12. Equation S4 indicates that the net interfacial ET rate of the system is closely related to the ET from the bulk to the interface.

At thermal equilibrium, the free electron concentration on the surface of semiconductor in the dark is

$$n_s = n_0 e^{-qV_s/k_B T} \quad (\text{S5})$$

where  $n_0$  is the thermal equilibrium free electron concentration in the bulk of the semiconductor,  $k_B$  is the Boltzmann constant,  $T$  is the absolute temperature in Kelvin, and  $q$  is the charge of electron. Equation S5 suggests that at thermal equilibrium without irradiation, the free electron concentration on the semiconductor surface is higher at a lower surface potential  $V_s$ . In the presence of irradiation, photoexcited electrons in the bulk of the semiconductor transfer to its surface and modify its surface potential as well as its surface free electron concentration. Photocatalytic processes can be regarded as closed circuits and the photogenerated electron injection is small in these processes, and therefore, the changes in surface potential and surface free electron concentration are negligible. In other words, we have  $n_s^{\text{light}} \approx n_s$  ( $n_s^{\text{light}}$  and  $n_s$  are the surface free electron concentrations under irradiation and at thermal equilibrium condition in the dark, respectively), and  $|\Delta V_s|/|V_s| \ll 1$ . Here  $\Delta V_s$  is the surface potential change in the semiconductor under illumination, i.e., the surface photovoltage. For a more general case, the surface free electron concentration and surface potential of the semiconductor are different from the corresponding values at thermal equilibrium, but Equation S5 is still valid, as long as the surface free electron concentration and the surface potential are taken as their corresponding steady state values.

We then investigate the interfacial ET behavior. A two-state ET model has been described by Marcus,<sup>39</sup> where the ET rate is determined by several microscopic parameters,  $k_0 = k_0(-\Delta G, H_{\text{DA}}, \lambda)$ , where  $-\Delta G = E_1 - E_2$ , is the so-called driving force (actually, it is an energy difference, and not a ‘force’; the mean force can be estimated from the relation  $-\Delta G/d$ , where  $d$  is the effective width of the interface layer), where  $E_1$  and  $E_2$  are the energies of Material 1 and Material 2 respectively,  $H_{\text{DA}}$  is the electronic coupling strength between Material

1 and Material 2, and  $\lambda$  is the reorganization energy. In a dual-band-gap photocatalyst, the energies of the two materials can be considered to be those of surface states with energy  $E_1 = E_{\text{CB}} + qV_s$  and  $E_2 = E'_{\text{CB}} + qV'_s$ ,<sup>12</sup> where  $E_{\text{CB}}$  and  $E'_{\text{CB}}$  are the energies of the bottom of the conduction band in the bulk of Material 1 and Material 2, respectively. The driving force can therefore be rewritten as  $-\Delta G = qV_s + E_{\text{CB}} - E_2 = q(V_s - V'_s) + \text{constant}$ . All of these microscopic parameters depend on the specific material structure, interface quality, and surface state wave functions, and can be obtained from experimental measurements, as well as from theoretical modeling calculations.<sup>40, 41</sup> As has been shown in previous reports, the ET rate increases with increasing driving force in the photocatalyst.<sup>42</sup>

For continuum electron occupation states, the two-state model has to be extended by integrating all possible occupation states:

$$k_{\text{ET}} = C \int_{-\infty}^{\infty} dE \rho(E) \int_{-\infty}^{\infty} dE' \rho'(E') k_0(H_{\text{DA}}, \lambda, (E + qV_s + E_{\text{CB}}) - (E' + qV'_s + E'_{\text{CB}})) \quad (\text{S6})$$

where  $C$  is a normalization constant,  $\rho(E)$  and  $\rho'(E')$  are the electron densities of states at the surfaces of the two materials, which satisfy the condition  $\int_{-\infty}^{\infty} dE \rho(E) = n_s$  and  $\int_{-\infty}^{\infty} dE' \rho'(E') = n'_s$ .

In our case, there is a high density of states on the RGO surface due to the presence of structural defects and oxygen-containing functional groups, so we suppose that the Fermi level of the RGO surface is pinned at a certain value, and thus  $\rho'(E') \approx \delta((E' + E'_{\text{CB}} + qV'_s) - E_{\text{final}})$ . According to Dirac function  $\int \delta(x - x^*) f(x) dx = f(x^*)$ , then we have

$$k_{\text{ET}} = C \int_{-\infty}^{\infty} dE \rho(E) k_0(H_{\text{DA}}, \lambda, E + qV_s + E_{\text{CB}} - E_{\text{final}}) \quad (\text{S7})$$

According to the mean value theorem for integrals, the ET rate can be written as

$$k_{\text{ET}} = n_s (qV_s) k_{0,n}(H_{\text{DA}}, \lambda, qV_s) \quad (\text{S8})$$

where  $k_{0,n}$  can be understood as an effective single electron transfer probability and Equation S8 thus means that the total ET rate is the product of the surface free electron concentration and the effective single electron transfer probability. Although Equation S8 is derived based on the

approximation of a pinned final state, it can be applied to more general cases by modifying the effective single electron transfer probability depending on the individual system under study.

Similarly, we express the hole transfer rate as

$$k_{\text{HT}} = p_s(-qV_s)k_{0,p}(H_{\text{DA}}, \lambda, -qV_s) \quad (\text{S9})$$

where  $p_s$  is the surface free hole concentration and  $k_{0,p}$  is the effective single hole transfer probability. Combining Equation S8 and S9, the interfacial charge transfer current density is

$$j_{\text{int}} = qn_s k_{0,n} - qp_s k_{0,p} \quad (\text{S10})$$

Without irradiation, the system is in equilibrium and there is no net charge current at the interface, i.e.,  $j_{\text{int}}^{\text{dark}} = qn_s k_{0,n} - qp_s k_{0,p} = 0$ . Under irradiation, the steady-state values of the different parameters will be changed. For photocatalysis, the interfacial properties do not change significantly after irradiation due to the fact that the charge carriers generated under irradiation corresponds to a low-level injection for the semiconductor, and we have  $k_{0,n}^{\text{light}} \approx k_{0,n}$  and  $k_{0,p}^{\text{light}} \approx k_{0,p}$ ; thus the interfacial CT photocurrent density is written as

$$j_{\text{int}}^{\text{light}} \approx q(n_s^{\text{light}} - n_s)k_{0,n} - q(p_s^{\text{light}} - p_s)k_{0,p} \quad (\text{S11})$$

where  $n_s^{\text{light}}$  is the surface free electron concentration under irradiation,  $p_s^{\text{light}}$  and  $p_s$  are the surface free hole concentrations under irradiation and in the dark, respectively, and  $k_{0,p}$  is the effective single hole transfer probability.



## References

1. Xu, Y.; Bai, H.; Lu, G.; Li, C.; Shi, G., Flexible Graphene Films via The Filtration of Water-soluble Noncovalent Functionalized Graphene Sheets. *J. Am. Chem. Soc.* **2008**, 130, (18), 5856-5857.
2. Yanhong, L.; Dejun, W.; Qidong, Z.; Min, Y.; Qinglin, Z., A Study of Quantum Confinement Properties of Photogenerated Charges in ZnO Nanoparticles by Surface Photovoltage Spectroscopy. *J. Phys. Chem. B* **2004**, 108, (10), 3202-3206.
3. Ravel, B.; Newville, M., ATHENA, ARTEMIS, HEPHAESTUS: Data Analysis for X-ray Absorption Spectroscopy Using IFEFFIT. *J. Synchrotron Rad.* **2005**, 12, (4), 537-541.
4. Rehr, J. J.; Kas, J. J.; Vila, F. D.; Prange, M. P.; Jorissen, K., Parameter-free Calculations of X-ray Spectra with FEFF9. *Phys. Chem. Chem. Phys.* **2010**, 12, (21), 5503-5513.
5. Dong, C.; Li, X.; Jin, P.; Zhao, W.; Chu, J.; Qi, J., Intersubunit Electron Transfer (IET) in Quantum Dots/Graphene Complex: What Features Does IET Endow the Complex with? *J. Phys. Chem. C* **2012**, 116, (29), 15833-15838.
6. Kresse, G.; Furthmüller, J., Efficiency of ab-initio Total Energy Calculations for Metals and Semiconductors Using a Plane-wave Basis Set. *Comput. Mater. Sci.* **1996**, 6, (1), 15-50.
7. Kresse, G.; Furthmüller, J., Efficient Iterative Schemes for ab initio Total-energy Calculations Using a Plane-wave Basis Set. *Phys. Rev. B* **1996**, 54, (16), 11169.
8. Hanus, L. H.; Sooklal, K.; Murphy, C. J.; Ploehn, H. J., Aggregation kinetics of dendrimer-stabilized CdS nanoclusters. *Langmuir* **2000**, 16, (6), 2621-2626.
9. Barick, K.; Aslam, M.; Dravid, V. P.; Bahadur, D., Self-aggregation and assembly of size-tunable transition metal doped ZnO nanocrystals. *J. Phys. Chem. C* **2008**, 112, (39), 15163-15170.
10. Feng, S.; Zhao, J.; Zhu, Z., Kinetically restraining aggregation of ZnS nanocrystals and the effect on photocatalysis. *Mater. Sci. Eng. B* **2008**, 150, (2), 116-120.
11. Hagfeldt, A.; Graetzel, M., Light-induced redox reactions in nanocrystalline systems. *Chem. Rev.* **1995**, 95, (1), 49-68.
12. Liu, E. K.; Zhu, B.S.; Luo, J.S., *Physics of Semiconductor*. 7th ed.; Publishing House of Electronics Industry: Beijing, 2008.
13. Moriya, M.; Minegishi, T.; Kumagai, H.; Katayama, M.; Kubota, J.; Domen, K., Stable Hydrogen Evolution from CdS-Modified CuGaSe<sub>2</sub> Photoelectrode under Visible-Light Irradiation. *J. Am. Chem. Soc.* **2013**, 135, (10), 3733-3735.
14. Frame, F. A.; Osterloh, F. E., CdSe-MoS<sub>2</sub>: a quantum size-confined photocatalyst for hydrogen evolution from water under visible light. *J. Phys. Chem. C* **2010**, 114, (23), 10628-10633.
15. Lin, Y.-Y.; Lee, H.-Y.; Ku, C.-S.; Chou, L.-W.; Wu, A. T., Bandgap Narrowing in High Dopant Tin Oxide Degenerate Thin Film Produced by Atmosphere Pressure Chemical Vapor Deposition. *Appl. Phys. Lett.* **2013**, 102, (11), 111912.
16. Wang, S.; Zhao, L.; Bai, L.; Yan, J.; Jiang, Q.; Lian, J., Enhancing Photocatalytic Activity of Disorder-engineered C/TiO<sub>2</sub> and TiO<sub>2</sub> Nanoparticles. *J. Mater. Chem. A* **2014**, 2, (20), 7439-7445.
17. Rabinovich, E.; Hodes, G., Effective Bandgap Lowering of CdS Deposited by Successive Ionic Layer Adsorption and Reaction. *J. Phys. Chem. C* **2013**, 117, (4), 1611-1620.
18. Kang, Q.; Cao, J.; Zhang, Y.; Liu, L.; Xu, H.; Ye, J., Reduced TiO<sub>2</sub> Nanotube Arrays for Photoelectrochemical Water Splitting. *J. Mater. Chem. A* **2013**, 1, (18), 5766-5774.
19. Chandramohan, S.; Kanjilal, A.; Tripathi, J. K.; Sarangi, S. N.; Sathyamoorthy, R.; Som,

T., Structural and Optical Properties of Mn-doped CdS Thin Films Prepared by Ion Implantation. *J. Appl. Phys.* **2009**, 105, (12), 123507.

20. Moustafa, M.; Zandt, T.; Janowitz, C.; Manzke, R., Growth and Band Gap Determination of the  $\text{ZrS}_x\text{Se}_{2-x}$  Single Crystal Series. *Phys. Rev. B* **2009**, 80, (3), 035206.

21. Podborska, A.; Gawel, B.; Pietrzak, Ł.; Szymańska, I. B.; Jeszka, J. K.; Łasocha, W.; Szaciłowski, K., Anomalous Photocathodic Behavior of CdS within the Urbach Tail Region. *J. Phys. Chem. C* **2009**, 113, (16), 6774-6784.

22. Banu Bahşi, Z.; Oral, A. Y., Effects of Mn and Cu Doping on The Microstructures and Optical Properties of Sol-gel Derived ZnO Thin Films. *Opt. Mater.* **2007**, 29, (6), 672-678.

23. Chen, Z.; Jaramillo, T. F.; Deutsch, T. G.; Kleiman-Shwarsstein, A.; Forman, A. J.; Gaillard, N.; Garland, R.; Takanabe, K.; Heske, C.; Sunkara, M., Accelerating materials development for photoelectrochemical hydrogen production: Standards for methods, definitions, and reporting protocols. *J. Mater. Res.* **2010**, 25, (1), 3-16.

24. Lee, D.; De Los Santos V, L.; Seo, J.; Felix, L. L.; Bustamante D, A.; Cole, J.; Barnes, C., The structure of graphite oxide: investigation of its surface chemical groups. *J. Phys. Chem. B* **2010**, 114, (17), 5723-5728.

25. Pham, V. H.; Cuong, T. V.; Hur, S. H.; Oh, E.; Kim, E. J.; Shin, E. W.; Chung, J. S., Chemical functionalization of graphene sheets by solvothermal reduction of a graphene oxide suspension in N-methyl-2-pyrrolidone. *J. Mater. Chem.* **2011**, 21, (10), 3371-3377.

26. Fan, W.; Lai, Q.; Zhang, Q.; Wang, Y., Nanocomposites of  $\text{TiO}_2$  and reduced graphene oxide as efficient photocatalysts for hydrogen evolution. *J. Phys. Chem. C* **2011**, 115, (21), 10694-10701.

27. Li, Y.; Wang, H.; Xie, L.; Liang, Y.; Hong, G.; Dai, H.,  $\text{MoS}_2$  nanoparticles grown on graphene: an advanced catalyst for the hydrogen evolution reaction. *J. Am. Chem. Soc.* **2011**, 133, (19), 7296-7299.

28. Xiang, Q.; Cheng, F.; Lang, D., Hierarchical Layered  $\text{WS}_2$ /Graphene-Modified CdS Nanorods for Efficient Photocatalytic Hydrogen Evolution. *ChemSusChem* **2016**, 9, (9), 996-1002.

29. Reber, J. F.; Rusek, M., Photochemical hydrogen production with platinized suspensions of cadmium sulfide and cadmium zinc sulfide modified by silver sulfide. *J. Phys. Chem.* **1986**, 90, (5), 824-834.

30. Kim, J.; Kim, F.; Huang, J., Seeing graphene-based sheets. *Mater. Today* **2010**, 13, (3), 28-38.

31. Li, D.; Müller, M. B.; Gilje, S.; Kaner, R. B.; Wallace, G. G., Processable aqueous dispersions of graphene nanosheets. *Nat. Nanotechnol.* **2008**, 3, (2), 101.

32. Robinson, J. T.; Tabakman, S. M.; Liang, Y.; Wang, H.; Sanchez Casalongue, H.; Vinh, D.; Dai, H., Ultrasmall Reduced Graphene Oxide with High Near-Infrared Absorbance for Photothermal Therapy. *J. Am. Chem. Soc.* **2011**, 133, (17), 6825-6831.

33. Li, Q.; Meng, H.; Yu, J.; Xiao, W.; Zheng, Y.; Wang, J., Enhanced Photocatalytic Hydrogen-Production Performance of Graphene- $\text{Zn}_x\text{Cd}_{1-x}\text{S}$  Composites by Using an Organic S Source. *Chem. Eur. J.* **2014**, 20, (4), 1176-1185.

34. Banu, N. N.; Ravichandran, K., Analysis of sulphur deficiency defect prevalent in SILAR-CdS films. *J. Mater. Sci. - Mater. Electron.* **2017**, 28, (16), 11584-11590.

35. Guillén, C.; Martínez, M.; Maffiotte, C.; Herrero, J., Chemistry of CdS/CuInSe<sub>2</sub> structures as controlled by the CdS deposition bath. *J. Electrochem. Soc.* **2001**, 148, (11), G602-G606.

36. Lightcap, I. V.; Kosel, T. H.; Kamat, P. V., Anchoring Semiconductor and Metal Nanoparticles on a Two-dimensional Catalyst Mat. Storing and Shuttling Electrons with Reduced Graphene Oxide. *Nano Lett.* **2010**, 10, (2), 577-83.
37. Wang, H.; Robinson, J. T.; Diankov, G.; Dai, H., Nanocrystal Growth on Graphene with Various Degrees of Oxidation. *J. Am. Chem. Soc.* **2010**, 132, (10), 3270-3271.
38. Li, J.; Tang, S.; Lu, L.; Zeng, H. C., Preparation of Nanocomposites of Metals, Metal oxides, and Carbon Nanotubes via Self-assembly. *J. Am. Chem. Soc.* **2007**, 129, (30), 9401-9409.
39. Marcus, R. A., Chemical and Electrochemical Electron-Transfer Theory. *Annu. Rev. Phys. Chem* **1964**, 15, (1), 155-196.
40. Vandewal, K., Interfacial Charge Transfer States in Condensed Phase Systems. *Annu. Rev. Phys. Chem* **2016**, 67, 113-133.
41. Zhu, H.; Yang, Y.; Wu, K.; Lian, T., Charge Transfer Dynamics from Photoexcited Semiconductor Quantum Dots. *Annu. Rev. Phys. Chem* **2016**, 67, 259-281.
42. Holmes, M. A.; Townsend, T. K.; Osterloh, F. E., Quantum Confinement Controlled Photocatalytic Water Splitting by Suspended CdSe Nanocrystals. *Chem. Commun.* **2012**, 48, (3), 371-373.